Topological electronic states in holey graphyne

Yong-Cheng Jiang,[1,2] Toshikaze Kariyado,[1] and Xiao Hu[1,2,*]

[1] *Research Center for Materials Nanoarchitectonics (MANA), National Institute for Materials Science (NIMS), Tsukuba 305-0044, Japan*

[2] *Graduate School of Science and Technology, University of Tsukuba, Tsukuba 305-8571, Japan*

Abstract

We unveil that the holey graphyne (HGY), a two-dimensional carbon allotrope where benzene rings are connected by two $-$C$\equiv$C$-$ bonds fabricated recently in a bottom-up way, exhibits topological electronic states. Using first-principles calculations and Wannier tight-binding modeling, we discover a higher-order topological invariant associated with C_2 symmetry of the material, and show that the resultant corner modes appear in nanoflakes matching to the structure of precursor reported previously, which are ready for direct experimental observations. In addition, we find that a band inversion between emergent g-like and h-like orbitals gives rise to a nontrivial topology characterized by $\mathbb{Z}_2$ invariant protected by an energy gap as large as 0.52 eV, manifesting helical edge states mimicking those in the prominent quantum spin Hall effect, which can be accessed experimentally after hydrogenation in HGY. We hope these findings trigger interests towards exploring the topological electronic states in HGY and related future electronics applications.

* HU.Xiao@nims.go.jp

1. INTRODUCTION

Haldane was the first to notice that a typical topological state, i.e., quantum Hall effect, can be realized without Landau levels induced by an external magnetic field. He developed a tight-binding (TB) model on honeycomb lattice with complex next-nearest-neighbor hoppings which break time-reversal symmetry (TRS) but introduce no net external magnetic field, generating quantum *anomalous* Hall effect characterized by a Chern number [1, 2]. Although this toy model was thought to be unrealistic at the time of the original proposal, soon after the discovery of graphene [3] it was pointed out by Kane and Mele that if spin-orbit coupling (SOC) is taken into account, graphene can be regarded as two copies of Haldane model, one for up spin and the other for down spin, manifesting the TRS-preserved quantum *spin* Hall effect (QSHE) characterized by a $\mathbb{Z}_2$ invariant [4, 5] (see also Ref. 6). However, the predicted QSHE is extremely hard to observe experimentally in graphene because of its very weak SOC. In order to resolve this issue, honeycomb systems with heavy elements have been investigated, aiming at having stronger SOC. Recently large-gap QSH insulators have been realized, in Bismuthene [7], monolayer 1T'-WTe_2 [8], stanene [9] and ultrathin Na_3Bi [10] for instance. For monolayer 1T'-WTe_2 with an energy gap $\sim$55 meV [11], the quantized edge conductance was observed in a transport channel of 100 nm up to 100 K [8]; while for the other materials, although energy gaps range from 0.3 eV to 0.8 eV, evidence for nontrivial topology is still limited in showing the local density of states (LDOS) for edge states, partially due to their small sample sizes below 40 nm. Despite all the noticeable progresses, further investigations are needed on materials possessing sizable energy gaps and amenable to fabrication into structures for device applications.

Besides utilizing strong SOC, deforming honeycomb lattice while preserving C_{6v} crystalline symmetry is also able to open a sizable gap in the Dirac dispersion associated with graphene structure, where the band inversion between bands with p- and d-like characters generates nontrivial topology [12–14]. This idea has been experimentally verified first in photonic crystals [15–19] due to their comparably easy fabrication, and later in electronic systems using *molecular graphene* [20], which is constructed by aligning carbon-monoxide molecules regularly on the Cu(111) surface in terms of the scanning tunneling microscopy (STM) technique [21, 22]. Such a superstructuring with C_{6v} symmetry can also generate corner modes originating from higher-order topology (HOT) [23], which has been

observed in various metamaterials [24–29] and electronic artificial lattices [30]. However, delicate deformations at the angstrom scale in real electronic materials are extremely difficult. While it was proposed that graphene with nanohole arrays [31] might reduce the difficulty, so far the top-down approach has not succeeded in fabricating nanohole arrays with desired patterns and scales. As the alternative approach, bottom-up synthesis methods have been tried, such as graphene nanoribbon [32], nanoporous graphene [33] and graphyne [34–36] with atomic precision, which yield interesting electronic [37–43] and mechanical properties [44]. Although topological corner modes have been predicted to exist in carbon allotropes such as graphyne [45] and graphdiyne [46], experimental observations have so far been limited.

Here, we unveil topological electronic states in the holey graphyne (HGY) fabricated recently in a bottom-up way [47] using first-principles calculations and Wannier TB modeling [48]. HGY is a two-dimensional (2D) carbon allotrope where benzene rings are connected by two $-\mathrm{C}{\equiv}\mathrm{C}-$ bonds (figure 1(a)). A nontrivial higher-order topological invariant is obtained from the C_2 symmetry of the material, and the resultant corner modes appear in nanoflakes with the edge morphology matching to the structure of precursor [47], which are ready for direct experimental observations. In addition, we find that intriguing molecular orbitals emerge in the hexagonal unit cell, and specially a band inversion between g-like and h-like modes gives rise to a nontrivial topology characterized by the $\mathbb{Z}_2$ topological invariant. In order to observe the helical edge states similar to those in QSHE, we propose in-plane hydrogenation in HGY to absorb the $p_{x,y}$ orbitals of carbon atoms in the pristine material, which opens a global topological energy gap at the appropriate energy and makes the helical edge states with opposite orbital angular momenta (OAM) observable in experiments.

2. METHODS

2.1. First-principles calculations

First-principles calculations are performed within the density-functional-theory (DFT) scheme using the Vienna *Ab initio* Simulation Package [49], where the projector augmented-wave method [50], the Perdew-Burke-Ernzerhof type generalized gradient approximation [51] for the exchange-correlation potential and a plane-wave basis set with a cutoff energy of 520 eV are adopted. A $11 \times 11 \times 1$ Γ-centered k-point mesh is used for both structure

relaxations and self-consistent calculations. The structure relaxations are performed until the Hellmann-Feynman forces acting on ions are smaller than 10^{-4} eV/Å and the energy tolerances are below 10^{-6} eV/atom. Graphyne sheets are separated by a vacuum layer of 2 nm, ensuring that interlayer couplings are negligible. The data post-processing is done using VASPKIT [52].

2.2. Wannier TB modeling

Maximally localized Wannier functions (MLWF) are obtained from data in first-principles calculations using WANNIER90 [53]. For HGY, the Wannier localization procedures are performed by projecting the eigenstates onto p_z orbitals on each atom and a superposition of p_x and p_y orbitals on atoms C' (figure 1(a)). The outer energy window is set as $E_{\text{out}} \in [-7 \text{ eV}, 12 \text{ eV}]$ to include all p orbitals, and the frozen energy window is set as $E_{\text{froz}} \in [-5.3 \text{ eV}, 2.4 \text{ eV}]$.

For hydrogenated HGY (HHGY), the projection orbitals are p_z orbitals on each carbon atom and bonding sp orbitals at the centers of C–H bonds. The outer energy window is the same as the case for HGY, while the frozen energy window starts from -4.5 eV to avoid other orbitals.

In the calculation of the HOT index γ (equation 4) for HGY, a pair of twist phases θ are introduced in a supercell consisting of 3×3 rhombic unit cells with periodic boundary conditions applied in two in-plane directions. For the ribbon structure of HHGY, the calculation is performed on a supercell composed of 20 hexagonal unit cells.

3. RESULTS AND DISCUSSIONS

3.1. Nontrivial higher-order topology and corner modes in HGY

By employing DFT calculations, we obtain the stable real-space structure of HGY with a lattice constant of $a_0 = 10.85$ Å (see bonding information in Supplementary Note S1) and the band structure as depicted in figures 1(a) and (b), respectively, in good agreement with the results in previous works [47, 54]. The structure in figure 1(a) can be regarded as a network of hexagons (benzene rings) and octagons, and there are two types of carbon sites, one belongs to the hexagon (shared with the octagon) and the other only belongs to the

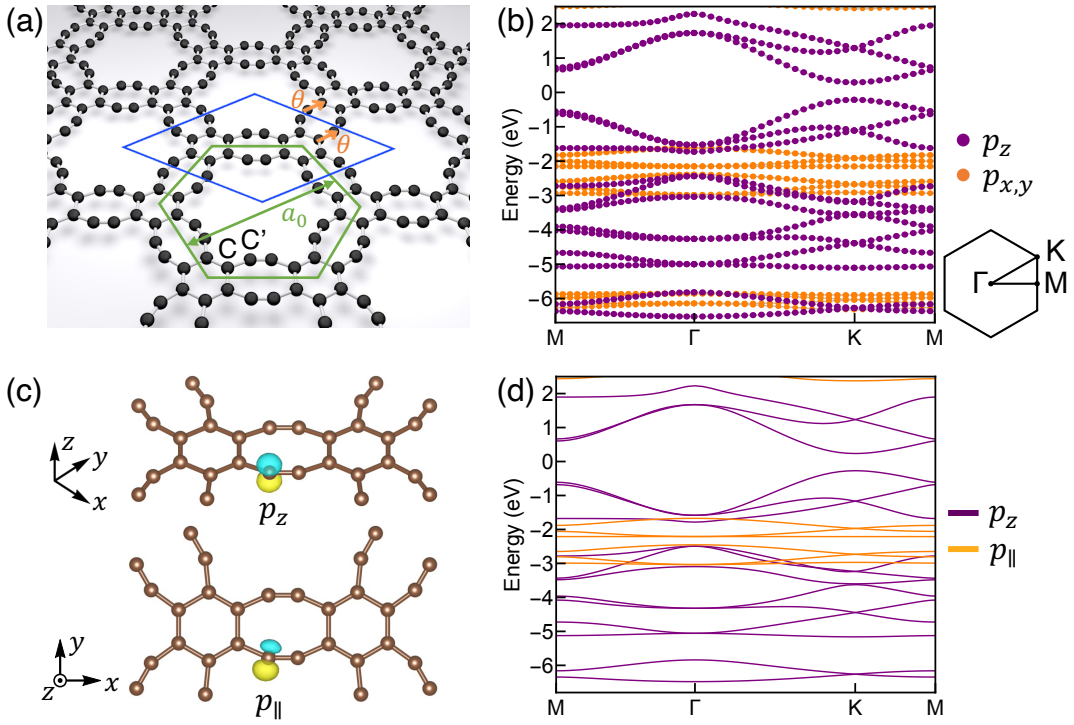

Figure 1. Holey graphyne (HGY) and its band structures. (a) Stable structure of HGY with lattice constant a_0 obtained by DFT calculations. Carbon atoms are divided into two types, C and C', where the former belongs to the benzene rings and the latter only belongs to the octagon. The rhombic unit cell corresponds to the precursor in the bottom-up synthesis as discovered in Ref. [47], whereas the hexagon denotes the highest symmetric unit cell. A pair of twist phases θ are introduced in the two bonds where the precursor is terminated for the calculation on the Berry phase γ for HOTI. (b) DFT band structure and the Brillouin zone. The Fermi energy is set to zero, and the eigenstates are projected to p_z and $p_{x,y}$ orbitals. (c) p_z-like and $p_\parallel$-like maximally localized Wannier functions obtained from the localization procedure, where the $p_\parallel$ orbital is the superposition of p_x and p_y orbitals. (d) Wannier-interpolated band structure obtained from the subspace selected by projecting onto p_z orbitals on each atom and $p_\parallel$ orbitals on atoms C'.

octagon. We name the former and the latter C and C', respectively. For the band structure in figure 1(b), we project the eigenstates onto the p_z and $p_{x,y}$ orbitals of carbon atoms, and find that occupations are either zero or unity, indicating no hybridization between them due to the mirror symmetry of the 2D material. The p_z orbital is also found orthogonal to the s orbital, and thus no hybridization occurs between these two orbitals. Therefore, the p_z

bands can be treated independently of other bands.

From the C_2 symmetry of the precursor octagon (see figure 1(a)), we surmise a HOT in the HGY. In order to explore the possibility, we first employ Wannier localization procedure to obtain the Wannier TB Hamiltonian. The MLWF shown in figure 1(c) indicate that p_z orbitals exist on each atom and a superposition of p_x and p_y orbitals exist on atoms C', which is named $p_\parallel$ because it forms the π bond parallel to the plane of the material. The Wannier-interpolated band structure is displayed in figure 1(d), which reproduces the DFT band structure shown in figure 1(b).

With the obtained Wannier TB Hamiltonian, we calculate the Berry phase γ for HOT insulator (HOTI) [55–57] associated with a pair of twist phases θ introduced on the two bonds of HGY as depicted in figure 1(a). The Hamiltonian $H(\theta)$ can be separated into two parts as

$$H(\theta) = h_0(\theta) + h_1, \tag{1}$$

$$h_0(\theta) = -t \sum_{\langle mn \rangle} (e^{i\theta} c_m^\dagger c_n + e^{-i\theta} c_n^\dagger c_m), \tag{2}$$

$$h_1 = -\sum_{mn} t_{mn} (c_m^\dagger c_n + c_n^\dagger c_m), \tag{3}$$

where $h_0(\theta)$ with nearest-neighbor hopping energy $t = 3.0$ eV obtained by MLWF is for the part with twist phases and h_1 is for the rest of the system including long-range hoppings. Note that since the phase twist is applied only on the selected bonds, this phase twist cannot be gauged out. The Berry phase for HOTI is defined as

$$\gamma = -i \int_0^{2\pi} \mathrm{d}\theta \langle \Psi(\theta) | \partial_\theta | \Psi(\theta) \rangle \pmod{2\pi} \tag{4}$$

with $|\Psi(\theta)\rangle$ being the ground state of $H(\theta)$. Since the system has the C_2 symmetry at the center of octagon, γ remains the same when $\theta \to -\theta$, i.e. $\gamma = -i \int_0^{-2\pi} \mathrm{d}\theta \langle \Psi(\theta) | \partial_\theta | \Psi(\theta) \rangle = -i \int_{2\pi}^0 \mathrm{d}\theta \langle \Psi(\theta) | \partial_\theta | \Psi(\theta) \rangle \pmod{2\pi}$, where we shift the integration by 2π since $H(\theta) = H(\theta + 2\pi)$. Knowing that the integration over a close loop $\theta = 0 \to 2\pi \to 0$ is 0 modulo 2π, γ is a $\mathbb{Z}_2$ index being either 0 or π. We find out

$$\gamma = \pi \quad \text{at the } \frac{9}{24} \text{ filling of } p_z \text{ bands}, \tag{5}$$

which corresponds to the filling upto the gap at -2.5 eV. Our calculation indicates clearly a nontrivial HOT in the HGY.

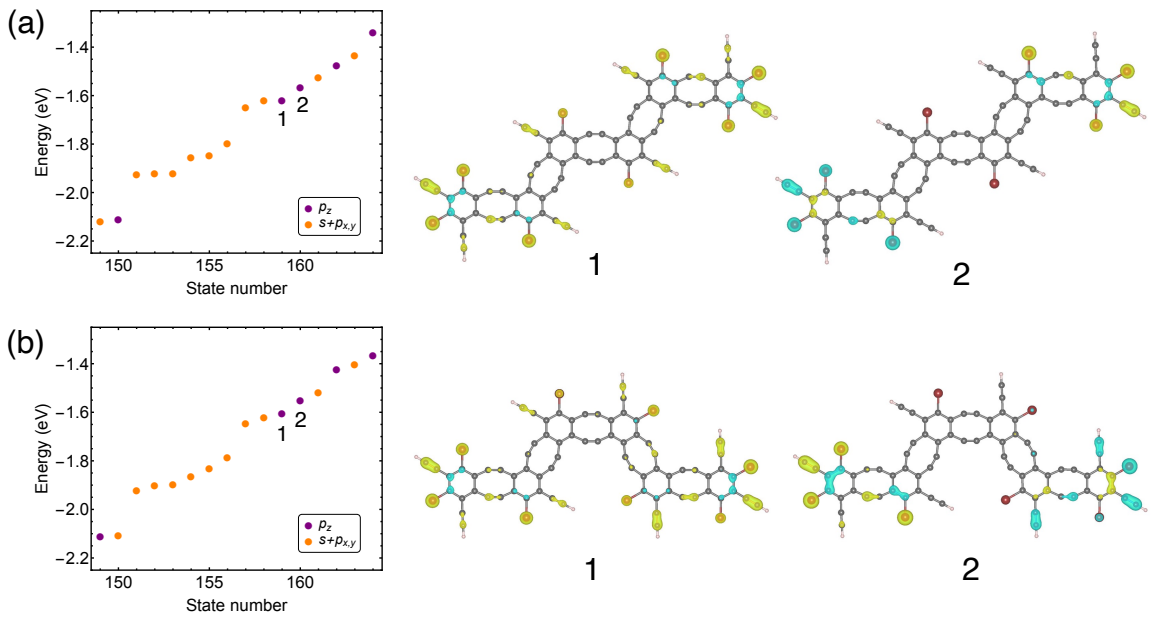

Figure 2. Topological corner modes in nanoflakes of HGY. (a) (left panel) Energy spectrum for the straight-type nanoflake with three rhombic unit cells and boundary morphology matching to the precursor. (right panel) Wave functions of the corner states 1 and 2. C, Br and H atoms are colored in gray, brown and pink, respectively. (b) Same as (a) except for the boomerang-type.

The nontrivial HOT will manifest corner modes in flake structures within the topological energy gap of p_z bands, which ranges from -2.5 eV to -1.8 eV. However, as can be seen in figure 1(b), this energy gap is covered by the $p_{x,y}$ bands, which hampers the observation of corner modes if the corner modes and the bulk states of $p_{x,y}$ orbitals are energetically close. In order to observe topological corner states arising from p_z orbital experimentally, the nanoflake should be small enough to have the bulk spectrum discretized, which makes it possible to distinguish the corner states from bulk states energetically.

Here we perform DFT calculations on two minimal nanoflakes consisting of three rhombic unit cells with boundary morphology exactly matching the precursor [47]. In the left panel of figure 2(a) we display the energy spectrum for the straight-type nanoflake. As shown in the right two panels of figure 2(a), the two states labeled by 1 and 2 formed by p_z orbital are corner states (see the other states of p_z orbital in Supplementary Note S2). The wave functions of the corner states possess even and odd C_2 parity with respect to the center of the nanoflake, respectively, corresponding to the bonding and antibonding states. The smallest energy difference between the antibonding corner state 2 and other states is 40 meV, which

is large enough for the STM technique to detect the corner states by measuring differential conductance ($\mathrm{d}I/\mathrm{d}V$) maps [40]. The bonding corner state 1 in figure 2(a) might be difficult to detect due to the small energy gap. Similarly, for the boomerang-type nanoflake, there also exist two corner states as shown in figure 2(b), and the antibonding corner state 2 can be detected by the STM. The antibonding corner states 2 in figure 2 have equal distributions of wave functions at two corners due to the C_2 symmetry and/or mirror symmetry of the nanoflake. When the Fermi energy is shifted to the energy of antibonding corner states 2, a fractional charge of $e/2$ is expected to appear at each corner.

3.2. Nontrivial first-order topology in HGY

We also investigate first-order topology which can be characterized by parity index (C_2 eigenvalue with respective to the center of hexagonal unit cell shown in figure 1(a)) [58]. For this purpose, we evaluate the parity index by counting the numbers of parity-even states at both Γ and M points ($N^+_{\Gamma/\mathrm{M}}$) for all the valence bands below the global bandgap at -2.4 eV and find $(N^+_\Gamma, N^+_\mathrm{M}) = (21, 21)$, which apparently suggests that the material is topologically trivial. However, it turns out that the topology of HGY is much richer than it looks at the first glance.

Since the p_z bands are independent of other bands as discussed in the previous section, we can extract the parity index for the p_z bands which gives $(N^+_\Gamma, N^+_\mathrm{M}) = (3, 5)$. This imbalance of parity index indicates the presence of nontrivial topology. Meanwhile, the parity index for the other bands, namely s and $p_{x,y}$ bands, is $(N^+_\Gamma, N^+_\mathrm{M}) = (18, 16)$. By checking the parity index in detail, we find out the imbalance originated from the three bands of $p_{x,y}$ orbitals around $E = -3$ eV, which give $(N^+_\Gamma, N^+_\mathrm{M}) = (3, 1)$. Therefore, HGY hosts two sets of topological bands, one from the p_z orbital and the other from the $p_{x,y}$ orbitals. Namely, these two orthogonal sets of bands exhibit nontrivial topology, showcasing rich topological characteristics in HGY.

Associated with the imbalance of parity index, we expect that the material manifests topological edge states within the energy gap of p_z bands around -2 eV (see figure 1(b)). Unfortunately, as can be seen in figure 1(d), these edge states are covered in energy by the bulk bands of $p_\parallel$ orbital although orthogonal to each other. In order to solve this issue, we consider in-plane hydrogenation on HGY, where hydrogen atoms are attached to carbon

atoms C'. The stable structure of HHGY with a lattice constant $a_0' = 11.02$ Å obtained by DFT calculations is illustrated in figure 3(a) (see bond lengths and angles in Supplementary Note S1). The DFT band structure is shown in figure 3(b), where a global energy gap of 0.52 eV is opened at the energy of -2 eV compared to the band structure of pristine HGY shown figure 1(b). Similar to the situation in HGY, the p_z bands in HHGY are orthogonal to other bands because of the mirror symmetry with respect to the horizontal plane. Therefore, we perform the Wannierization procedure by projecting the eigenstates onto p_z orbitals on each carbon atom, and the interpolated band structure is shown in figure 3(c), reproducing the p_z bands obtained by DFT calculations shown in figure 3(b).

We display the projected density of states (PDOS) for HHGY in figure 3(d), where the $p_{x,y}$ orbitals of carbon atoms and the s orbital of hydrogen atoms exist below the bandgap at -2 eV. This is in sharp contrast to the situation in HGY where the $p_{x,y}$ orbitals fill up almost all the bandgap of p_z orbital as displayed in figure 1(b). The in-plane hydrogenation leads to the sp-hybridization between the $p_{x,y}$ orbitals of carbon atoms and the s orbital of hydrogen atoms, lowering the energy of the original $p_\parallel$ orbital. Therefore, the hydrogenation effectively kills the original $p_\parallel$ orbital and results in an energy gap as large as 0.52 eV.

In order to double-check our strategy, we re-examine the topology for the p_z bands using parity index, and find imbalance by $(N_\Gamma^+, N_\mathrm{M}^+) = (3, 5)$ for the states below the energy gap, indicating the presence of nontrivial topology as expected (see Supplementary Note S3). We can also check the parity index for all states including other orbitals, which gives $(N_\Gamma^+, N_\mathrm{M}^+) = (24, 26)$, meaning that the nontrivial topology originates purely from the p_z bands as discussed above.

Moreover, in figures 3(b) and (c) we notice that the unbalanced parity index is induced by a band inversion between g- and h-like modes around the bandgap at the Γ point. As illustrated in figures 3(e) and (f), the eigenstates g-, h- and i-like modes are named by counting the number of nodes along the perimeter of hexagonal unit cell, i.e., 8, 10, and 12, with even, odd and even parity, respectively. Note that if the green hexagonal cell in figure 3(a) is isolated and the hoppings between p_z orbitals are uniform, the classification by the number of nodes is exact and the eigenenergy should increase with the number of nodes. However, in figure 3(b), g-like mode comes above h-like mode, signaling a band inversion. For the two isolated valence p_z bands with h-like mode with odd parity at the Γ point and parity-even states at the M point, we evaluate the Wilson loop [2, 59] and find a phase

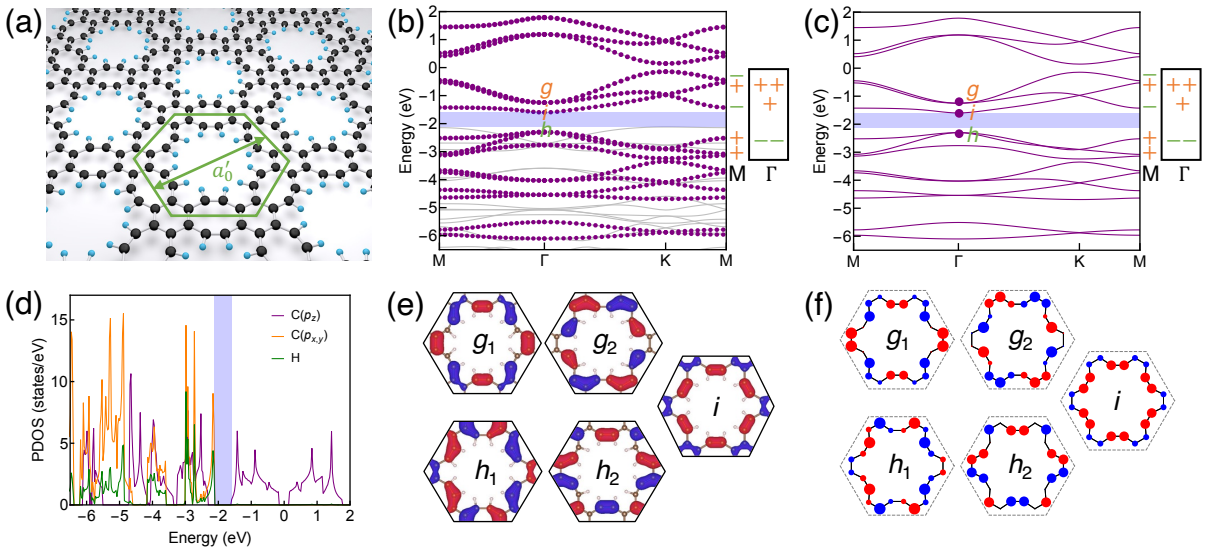

Figure 3. Hydrogenated holey graphyne (HHGY) and its band structures. (a) Stable structure of HHGY with lattice constant a_0' obtained by DFT calculations, where carbon and hydrogen atoms are colored in black and cyan, respectively. The unit cell with the highest symmetry is denoted by a hexagon. (b) Band structures obtained by DFT calculations, with eigenstates projected to p_z orbitals and the bandgap shown by a region highlighted in blue. The g-, i- and h-like modes are labeled explicitly, and the parity of the eigenstates at Γ and M points for the corresponding five bands are denoted by plus and minus signs. (c) Same as (b) except for Wannier interpolation which is performed by projecting onto p_z orbitals on each carbon atom. (d) Projected density of states (PDOS) obtained by DFT calculations, with the bandgap shown by a region highlighted in blue. (e) Wave functions of g-, h- and i-like modes at the Γ point obtained by DFT calculations, with red/blue color denoting the plus/minus value. Notation: $g_1 \equiv g_{x^4-6x^2y^2+y^4}$, $g_2 \equiv g_{xy(x^2-y^2)}$, $h_1 \equiv h_{x(x^4-10x^2y^2+5y^4)}$, $h_2 \equiv h_{y(5x^4-10x^2y^2+y^4)}$, $i \equiv i_{x^6-15x^4y^2+15x^2y^4-y^6}$. (f) Same as (e) except for Wannier interpolation, with amplitude represented by size of dots.

winding of 2π, which indicates a nontrivial band topology (see Supplementary Note S4).

Coming back to the full argument with the actual crystalline symmetry, doubly degenerate g- and h-like modes are the 2D irreducible representations of the C_{6v} symmetry in the material, while the singlet i-like mode is the 1D irreducible representation. With the double degeneracy, we can construct pseudospin states using g- and h-like modes:

$$|g_\pm\rangle = \frac{1}{\sqrt{2}}\left(|g_1\rangle \pm i|g_2\rangle\right), \quad |h_\pm\rangle = \frac{1}{\sqrt{2}}\left(|h_1\rangle \pm i|h_2\rangle\right). \tag{6}$$

We regard $|g_+\rangle$ and $|h_+\rangle$ as pseudospin-up states, since their phases of wave functions increase $+8\pi$ and $+10\pi$ counterclockwisely along the perimeter of hexagonal unit cell, which correspond to the states with OAM $+4\hbar$ and $+5\hbar$, respectively, noting that the operator of OAM is $-i\hbar\frac{\partial}{\partial\phi}$. The time-reversal counterparts $|g_-\rangle$ and $|h_-\rangle$ are regarded as pseudospin-down states with OAM $-4\hbar$ and $-5\hbar$, respectively. Again, this argument is exact in the case of an isolated cell with a uniform hopping. In this system where there is only C_{6v} symmetry, the eigenstates are classified by OAM up to mod $6\hbar$, and $\pm4\hbar$ and $\pm5\hbar$ correspond to $\mp2\hbar$ and $\mp\hbar$, respectively.

3.3. Helical edge states in a ribbon of HHGY

The nontrivial topology characterized by the $\mathbb{Z}_2$ topological index will manifest topological edge states. As can be seen in figure 4(a) obtained by the Wannier TB calculations on the ribbon structure with a molecule-zigzag edge morphology [14] where the hexagonal unit cells remain intact, a pair of topological edge states carrying opposite pseudospins appear within the DFT bulk bandgap (see Supplementary Notes S5 for details). The LDOS of edge states are shown in figure 4(b) (for detailed understanding see Supplementary Notes S6), and the wave functions including phases with comparison to the bulk pseudospin states $|\pm\rangle$ $(= (|g_\pm\rangle \pm i|h_\pm\rangle)/\sqrt{2})$ are shown in figure 4(c).

It should be noted that, in the previous work [43] the topological control means real-space geometrical control, namely changing neck widths between holes in holey graphene; no topology in momentum space has been touched. In the present work, the topology is related to Berry phase defined by Bloch wave functions in momentum space, and we show successfully that this can be engineered by real-space control, such as arrangement of precursors and/or edge morphology of ribbon.

A direct comparison between figures 2(a) and 4(a) is difficult, since they stand for two different systems with energy shift: figure 2(a) for small nanoflakes without hydrogenation, whereas figure 4(a) for a ribbon with hydrogenation. The edge morphology exhibiting the topological edge states in this work cannot be achieved by the available precursor directly, and thus trials on edge treatments are required, such as out-of-plane hydrogenation.

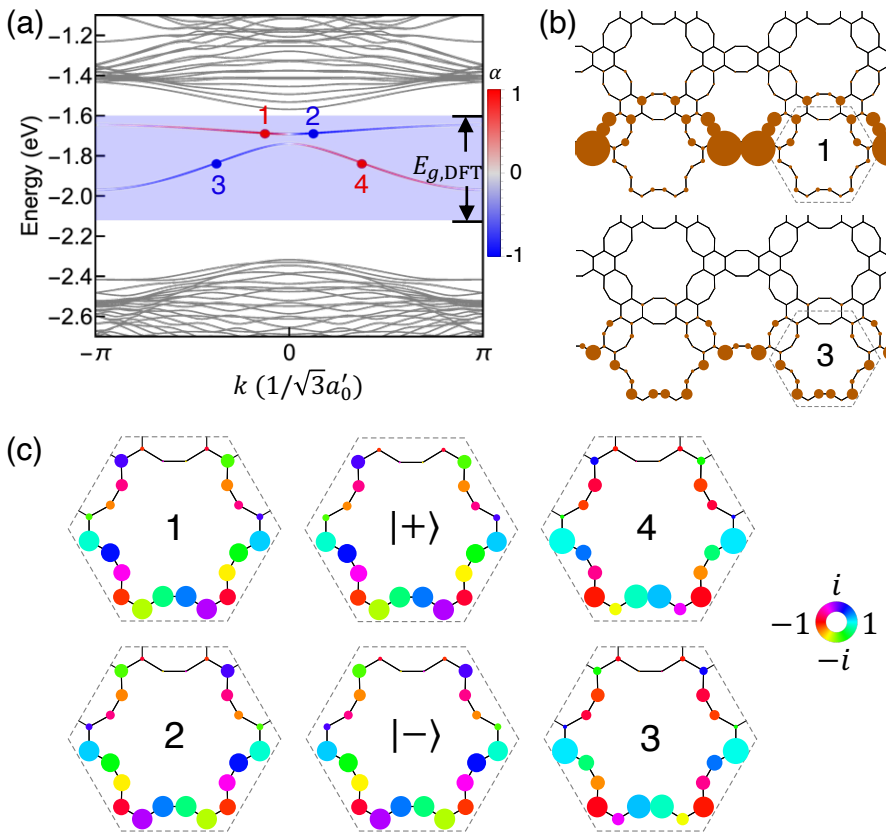

Figure 4. Topological edge states in a ribbon of HHGY. (a) Energy dispersion of a ribbon of HHGY obtained by Wannier TB calculations on p_z orbitals. The region highlighted in blue represents the DFT bulk bandgap, where the edge states are colored by their pseudospin polarizations α (see Supplementary Note S5). (b) LDOS $|\psi_i|^2$ for the edge state 1 (upper panel) and 3 (lower panel) as labeled in (a), with the outmost unit cell highlighted by a dashed hexagon. (c) Comparison between the bulk pseudospin states $|\pm\rangle$ and the wave functions with spinful parts in the outmost unit cell of the four edge states 1 to 4, with amplitude and phase denoted by size and color of dots, respectively.

4. CONCLUSIONS

In summary, we uncover topological electronic states in holey graphyne, through DFT calculations and Wannier TB modeling. Firstly, a nontrivial $\mathbb{Z}_2$ higher-order topological invariant is obtained arising from the C_2 symmetry of the material. We display explicitly the minimal nanoflakes hosting the corresponding corner states, which can be fabricated using the same precursor in the experiment [47], and the corner modes are ready to be observed

by measuring differential conductance maps using STM. While so far the observation of topological corner modes in electronic systems has been limited to artificial lattices made by positioning carbon-monoxide molecules on Cu(111) surface [30], holey graphyne could be the non-artificial material where topological electronic corner modes are experimentally observed. Secondly, by introducing an in-plane hydrogenation, holey graphyne opens a large energy gap of 0.52 eV at -2 eV, with a nontrivial topology arising from the band inversion between g- and h-like modes and characterized by a $\mathbb{Z}_2$ invariant. Topological edge states carrying opposite OAMs propagate in opposite directions, indicating potential applications in orbitronic devices with low energy loss workable at room temperature. Our work points out that holey graphyne serves as an ideal platform to observe topological electronic corner modes and edge states with OAMs protected by a large energy gap, opening a new avenue for further investigation and exploitation of topology in 2D carbon allotropes for both scientific understanding and practical applications.

ACKNOWLEDGEMENT

This work is supported by CREST, JST (Core Research for Evolutionary Science and Technology, Japan Science and Technology Agency) (Grant Number JPMJCR18T4).

DATA AVAILABILITY STATEMENT

All the data that support the findings of this study are available from the corresponding author upon reasonable request, following the policy of JST.

---

[1] F. D. M. Haldane, Model for a Quantum Hall Effect without Landau Levels: Condensed-Matter Realization of the "Parity Anomaly", Phys. Rev. Lett. **61**, 2015 (1988).

[2] H. Weng, R. Yu, X. Hu, X. Dai, and Z. Fang, Quantum anomalous Hall effect and related topological electronic states, Adv. Phys. **64**, 227 (2015).

[3] A. H. Castro Neto, F. Guinea, N. M. R. Peres, K. S. Novoselov, and A. K. Geim, The electronic properties of graphene, Rev. Mod. Phys. **81**, 109 (2009).

[4] C. L. Kane and E. J. Mele, Z_2 Topological Order and the Quantum Spin Hall Effect, Phys. Rev. Lett. **95**, 146802 (2005).

[5] C. L. Kane and E. J. Mele, Quantum Spin hall effect in graphene, Phys. Rev. Lett. **95**, 226801 (2005).

[6] B. A. Bernevig, T. L. Hughes, and S.-C. Zhang, Quantum Spin Hall Effect and Topological Phase Transition in HgTe Quantum Wells, Science **314**, 1757 (2006).

[7] F. Reis, G. Li, L. Dudy, M. Bauernfeind, S. Glass, W. Hanke, R. Thomale, J. Schäfer, and R. Claessen, Bismuthene on a SiC substrate: A candidate for a high-temperature quantum spin Hall material, Science **357**, 287 (2017).

[8] S. Wu, V. Fatemi, Q. D. Gibson, K. Watanabe, T. Taniguchi, R. J. Cava, and P. Jarillo-Herrero, Observation of the quantum spin Hall effect up to 100 kelvin in a monolayer crystal, Science **359**, 76 (2018).

[9] J. Deng, B. Xia, X. Ma, H. Chen, H. Shan, X. Zhai, B. Li, A. Zhao, Y. Xu, W. Duan, S.-C. Zhang, B. Wang, and J. G. Hou, Epitaxial growth of ultraflat stanene with topological band inversion, Nat. Mater. **17**, 1081 (2018).

[10] J. L. Collins, A. Tadich, W. Wu, L. C. Gomes, J. N. B. Rodrigues, C. Liu, J. Hellerstedt, H. Ryu, S. Tang, S.-K. Mo, S. Adam, S. A. Yang, M. S. Fuhrer, and M. T. Edmonds, Electric-field-tuned topological phase transition in ultrathin Na_3Bi, Nature **564**, 390 (2018).

[11] S. Tang, C. Zhang, D. Wong, Z. Pedramrazi, H.-Z. Tsai, C. Jia, B. Moritz, M. Claassen, H. Ryu, S. Kahn, J. Jiang, H. Yan, M. Hashimoto, D. Lu, R. G. Moore, C.-C. Hwang, C. Hwang, Z. Hussain, Y. Chen, M. M. Ugeda, Z. Liu, X. Xie, T. P. Devereaux, M. F. Crommie, S.-K. Mo, and Z.-X. Shen, Quantum spin Hall state in monolayer $1T'$-WTe_2, Nat. Phys. **13**, 683 (2017).

[12] L.-H. Wu and X. Hu, Scheme for Achieving a Topological Photonic Crystal by Using Dielectric Material, Phys. Rev. Lett. **114**, 223901 (2015).

[13] L.-H. Wu and X. Hu, Topological Properties of Electrons in Honeycomb Lattice with Detuned Hopping Energy, Sci. Rep. **6**, 24347 (2016).

[14] T. Kariyado and X. Hu, Topological States Characterized by Mirror Winding Numbers in Graphene with Bond Modulation, Sci. Rep. **7**, 16515 (2017).

[15] Y. Yang, Y. F. Xu, T. Xu, H.-X. Wang, J.-H. Jiang, X. Hu, and Z. H. Hang, Visualization of a Unidirectional Electromagnetic Waveguide Using Topological Photonic Crystals Made of

Dielectric Materials, Phys. Rev. Lett. **120**, 217401 (2018).

[16] Y. Li, Y. Sun, W. Zhu, Z. Guo, J. Jiang, T. Kariyado, H. Chen, and X. Hu, Topological LC-circuits based on microstrips and observation of electromagnetic modes with orbital angular momentum, Nat. Commun. **9**, 4598 (2018).

[17] S. Barik, A. Karasahin, C. Flower, T. Cai, H. Miyake, W. DeGottardi, M. Hafezi, and E. Waks, A topological quantum optics interface, Science **359**, 666 (2018).

[18] N. Parappurath, F. Alpeggiani, L. Kuipers, and E. Verhagen, Direct observation of topological edge states in silicon photonic crystals: Spin, dispersion, and chiral routing, Sci. Adv. **6**, eaaw4137 (2020).

[19] X.-X. Wang, Z. Guo, J. Song, H. Jiang, H. Chen, and X. Hu, Unique Huygens-Fresnel electromagnetic transportation of chiral Dirac wavelet in topological photonic crystal, Nat. Commun. **14**, 3040 (2023).

[20] S. E. Freeney, J. J. van den Broeke, A. J. J. Harsveld van der Veen, I. Swart, and C. Morais Smith, Edge-Dependent Topology in Kekulé Lattices, Phys. Rev. Lett. **124**, 236404 (2020).

[21] K. K. Gomes, W. Mar, W. Ko, F. Guinea, and H. C. Manoharan, Designer Dirac fermions and topological phases in molecular graphene, Nature **483**, 306 (2012).

[22] M. Polini, F. Guinea, M. Lewenstein, H. C. Manoharan, and V. Pellegrini, Artificial honeycomb lattices for electrons, atoms and photons, Nat. Nanotechnol. **8**, 625 (2013).

[23] W. A. Benalcazar, B. A. Bernevig, and T. L. Hughes, Quantized electric multipole insulators, Science **357**, 61 (2017).

[24] J. Noh, W. A. Benalcazar, S. Huang, M. J. Collins, K. P. Chen, T. L. Hughes, and M. C. Rechtsman, Topological protection of photonic mid-gap defect modes, Nat. Photonics **12**, 408 (2018).

[25] M. Serra-Garcia, V. Peri, R. Süsstrunk, O. R. Bilal, T. Larsen, L. G. Villanueva, and S. D. Huber, Observation of a phononic quadrupole topological insulator, Nature **555**, 342 (2018).

[26] C. W. Peterson, W. A. Benalcazar, T. L. Hughes, and G. Bahl, A quantized microwave quadrupole insulator with topologically protected corner states, Nature **555**, 346 (2018).

[27] S. Imhof, C. Berger, F. Bayer, J. Brehm, L. W. Molenkamp, T. Kiessling, F. Schindler, C. H. Lee, M. Greiter, T. Neupert, and R. Thomale, Topolectrical-circuit realization of topological corner modes, Nat. Phys. **14**, 925 (2018).

[28] H. Xue, Y. Yang, F. Gao, Y. Chong, and B. Zhang, Acoustic higher-order topological insulator on a kagome lattice, Nat. Mater. **18**, 108 (2019).

[29] S. Mittal, V. V. Orre, G. Zhu, M. A. Gorlach, A. Poddubny, and M. Hafezi, Photonic quadrupole topological phases, Nat. Photonics **13**, 692 (2019).

[30] S. N. Kempkes, M. R. Slot, J. J. van den Broeke, P. Capiod, W. A. Benalcazar, D. Vanmaekelbergh, D. Bercioux, I. Swart, and C. Morais Smith, Robust zero-energy modes in an electronic higher-order topological insulator, Nat. Mater. **18**, 1292 (2019).

[31] T. Kariyado, Y.-C. Jiang, H. Yang, and X. Hu, Counterpropagating topological interface states in graphene patchwork structures with regular arrays of nanoholes, Phys. Rev. B **98**, 195416 (2018).

[32] J. Cai, P. Ruffieux, R. Jaafar, M. Bieri, T. Braun, S. Blankenburg, M. Muoth, A. P. Seitsonen, M. Saleh, X. Feng, K. Müllen, and R. Fasel, Atomically precise bottom-up fabrication of graphene nanoribbons, Nature **466**, 470 (2010).

[33] C. Moreno, M. Vilas-Varela, B. Kretz, A. Garcia-Lekue, M. V. Costache, M. Paradinas, M. Panighel, G. Ceballos, S. O. Valenzuela, D. Peña, and A. Mugarza, Bottom-up synthesis of multifunctional nanoporous graphene, Science **360**, 199 (2018).

[34] M. M. Haley, Synthesis and properties of annulenic subunits of graphyne and graphdiyne nanoarchitectures, Pure Appl. Chem. **80**, 519 (2008).

[35] G. Li, Y. Li, H. Liu, Y. Guo, Y. Li, and D. Zhu, Architecture of graphdiyne nanoscale films, Chem. Commun. **46**, 3256 (2010).

[36] Y. Hu, C. Wu, Q. Pan, Y. Jin, R. Lyu, V. Martinez, S. Huang, J. Wu, L. J. Wayment, N. A. Clark, M. B. Raschke, Y. Zhao, and W. Zhang, Synthesis of γ-graphyne using dynamic covalent chemistry, Nat. Synth. **1**, 449 (2022).

[37] Y.-W. Son, M. L. Cohen, and S. G. Louie, Half-metallic graphene nanoribbons, Nature **444**, 347 (2006).

[38] Y.-W. Son, M. L. Cohen, and S. G. Louie, Energy Gaps in Graphene Nanoribbons, Phys. Rev. Lett. **97**, 216803 (2006).

[39] L. D. Pan, L. Z. Zhang, B. Q. Song, S. X. Du, and H.-J. Gao, Graphyne- and graphdiyne-based nanoribbons: Density functional theory calculations of electronic structures, Appl. Phys. Lett. **98**, 173102 (2011).

[40] D. J. Rizzo, G. Veber, T. Cao, C. Bronner, T. Chen, F. Zhao, H. Rodriguez, S. G. Louie, M. F. Crommie, and F. R. Fischer, Topological band engineering of graphene nanoribbons, Nature **560**, 204 (2018).

[41] H. Huang, H. Shi, P. Das, J. Qin, Y. Li, X. Wang, F. Su, P. Wen, S. Li, P. Lu, F. Liu, Y. Li, Y. Zhang, Y. Wang, Z.-S. Wu, and H.-M. Cheng, The Chemistry and Promising Applications of Graphene and Porous Graphene Materials, Adv. Funct. Mater. **30**, 1909035 (2020).

[42] D. Singh, V. Shukla, and R. Ahuja, Optical excitations and thermoelectric properties of two-dimensional holey graphene, Phys. Rev. B **102**, 075444 (2020).

[43] P. V. Barkov and O. E. Glukhova, Holey Graphene: Topological Control of Electronic Properties and Electric Conductivity, Nanomaterials **11**, 1074 (2021).

[44] S. W. Cranford and M. J. Buehler, Mechanical properties of graphyne, Carbon **49**, 4111 (2011).

[45] B. Liu, G. Zhao, Z. Liu, and Z. F. Wang, Two-Dimensional Quadrupole Topological Insulator in γ-Graphyne, Nano Lett. **19**, 6492 (2019).

[46] X.-L. Sheng, C. Chen, H. Liu, Z. Chen, Z.-M. Yu, Y. X. Zhao, and S. A. Yang, Two-Dimensional Second-Order Topological Insulator in Graphdiyne, Phys. Rev. Lett. **123**, 256402 (2019).

[47] X. Liu, S. M. Cho, S. Lin, Z. Chen, W. Choi, Y.-M. Kim, E. Yun, E. H. Baek, D. H. Ryu, and H. Lee, Constructing two-dimensional holey graphyne with unusual annulative π-extension, Matter **5**, 2306 (2022).

[48] N. Marzari, A. A. Mostofi, J. R. Yates, I. Souza, and D. Vanderbilt, Maximally localized Wannier functions: Theory and applications, Rev. Mod. Phys. **84**, 1419 (2012).

[49] G. Kresse and J. Furthmüller, Efficient iterative schemes for ab initio total-energy calculations using a plane-wave basis set, Phys. Rev. B **54**, 11169 (1996).

[50] G. Kresse and D. Joubert, From ultrasoft pseudopotentials to the projector augmented-wave method, Phys. Rev. B **59**, 1758 (1999).

[51] J. P. Perdew, K. Burke, and M. Ernzerhof, Generalized Gradient Approximation Made Simple, Phys. Rev. Lett. **77**, 3865 (1996).

[52] V. Wang, N. Xu, J.-C. Liu, G. Tang, and W.-T. Geng, VASPKIT: A user-friendly interface facilitating high-throughput computing and analysis using VASP code, Comput. Phys. Commun. **267**, 108033 (2021).

[53] G. Pizzi, V. Vitale, R. Arita, S. Blügel, F. Freimuth, G. Géranton, M. Gibertini, D. Gresch, C. Johnson, T. Koretsune, J. Ibañez-Azpiroz, H. Lee, J.-M. Lihm, D. Marchand, A. Marrazzo, Y. Mokrousov, J. I. Mustafa, Y. Nohara, Y. Nomura, L. Paulatto, S. Poncé, T. Ponweiser, J. Qiao, F. Thöle, S. S. Tsirkin, M. Wierzbowska, N. Marzari, D. Vanderbilt, I. Souza, A. A. Mostofi, and J. R. Yates, Wannier90 as a community code: new features and applications, J. Phys. Condens. Matter **32**, 165902 (2020).

[54] M. Sajjad, S. S. Nair, Y. A. Samad, and N. Singh, Colossal figure of merit and compelling HER catalytic activity of holey graphyne, Sci. Rep. **13**, 9123 (2023).

[55] T. Mizoguchi, H. Araki, and Y. Hatsugai, Higher-Order Topological Phase in a Honeycomb-Lattice Model with Anti-Kekulé Distortion, J. Phys. Soc. Jpn. **88**, 104703 (2019).

[56] K. Kudo, T. Yoshida, and Y. Hatsugai, Higher-Order Topological Mott Insulators, Phys. Rev. Lett. **123**, 196402 (2019).

[57] H. Araki, T. Mizoguchi, and Y. Hatsugai, $\mathbb{Z}_Q$ Berry phase for higher-order symmetry-protected topological phases, Phys. Rev. Res. **2**, 012009(R) (2020).

[58] W. A. Benalcazar, J. C. Y. Teo, and T. L. Hughes, Classification of two-dimensional topological crystalline superconductors and Majorana bound states at disclinations, Phys. Rev. B **89**, 224503 (2014).

[59] R. Yu, X. L. Qi, A. Bernevig, Z. Fang, and X. Dai, Equivalent expression of Z_2 topological invariant for band insulators using the non-Abelian Berry connection, Phys. Rev. B **84**, 75119 (2011).